Delocalised electron-holes on oxygen in a battery cathode

Robert A. House[1,*], Gregory J. Rees[1], Kit McColl[2], John-Joseph Marie[1], Mirian Garcia-Fernandez[3], Abhishek Nag[3], Kejin-Zhou[3], Simon Cassidy[4], Benjamin Morgan[2], M. Saiful Islam[1], Peter G. Bruce[1,4,*]

[1]Department of Materials, University of Oxford, Parks Road, Oxford, OX1 3PH, U.K.
[2]Department of Chemistry, University of Bath, Bath, BA2 7AY, UK
[3]Diamond Light Source, Harwell, UK
[4]Department of Chemistry, University of Oxford, Inorganic Chemistry Laboratory, South Parks Road, Oxford OX1 3QR, U.K.
*Corresponding authors: robert.house@materials.ox.ac.uk, peter.bruce@materials.ox.ac.uk

Abstract

Oxide ions in transition metal oxide materials can store charge at high voltage offering one of the very few routes to battery cathodes with higher energy density. However, oxidation of O^{2-} on charging is accompanied by condensation of oxidised oxide ions to form molecular O_2 trapped in the material; as a consequence, the discharge voltage is much lower than charge, leading to undesirable voltage hysteresis. Here, we capture the nature of the electron-holes on O^{2-} before O_2 formation, by exploiting the suppressed transition metal rearrangement in ribbon-ordered $Na_{0.6}[Li_{0.2}Mn_{0.8}]O_2$. We show using SQUID, ^{17}O NMR, DFT and RIXS that the electron-holes formed on oxidation of O^{2-} are delocalised and distributed across the oxide ions coordinated to two Mn (O-Mn_2) that are arranged in ribbons in the transition metal layers. Furthermore, we track these delocalised hole states as they gradually localise in the structure in the form of trapped molecular O_2, over a period of days. Establishing the nature of hole states on oxide ions is important if truly reversible O-redox cathodes, with the same voltage on charge and discharge, are to be realised and used to increase the energy density of lithium batteries.

Introduction

Achieving a step-change in the energy density of rechargeable Li and Na-ion batteries is hindered by the limitations of the cathode. Conventional transition metal oxide cathode materials, such as $LiMn_2O_4$, operate by the removal on charge, and reinsertion, on discharge, of Li^+, charge-compensated through the oxidation and reduction of the transition metal ions, which imposes a limit on the capacity to store charge. However, in the class of so-called 'O-redox' cathodes, exemplified by the layered lithium-rich transition metal oxide $Li[Li_{0.2}Ni_{0.13}Co_{0.13}Mn_{0.54}]O_2$, Li^+ can be extracted on charge beyond the limit of transition metal oxidation, by oxidation of the O^{2-} ions, providing vital additional capacity at high voltage.[1–12] O-redox cathodes offer one of the very few routes to increase the energy density of lithium and sodium batteries, a key challenge in the field.[13–17]

Understanding the nature of oxidised oxygen in transition metal oxides has proved very difficult. It has been shown recently that oxidation of oxide ions triggers migration of the transition metal ions forming voids that enable condensation of the O to molecular O_2 trapped inside the structure, resulting in a significant voltage loss on subsequent discharge.[18–20]

As a result of the structural reorganisation, it has not proved possible to capture the nature of the hole states on O^{2-} before they form O_2. Preserving the hole states on O^{2-} and preventing O_2 formation is essential if voltage loss is to be avoided and a truly reversible, high voltage O-redox plateau is to be achieved, an important goal in the field. We recently demonstrated that structural reorganisation and hence O_2 formation, can be frustrated by controlling the superstructure ordering of the transition metal ions in the transition metal layers.[21] $Na_{0.6}[Li_{0.2}Mn_{0.8}]O_2$ possesses a different transition metal superstructure to the honeycomb ordering present in most O-redox materials.[21–26] As a result, voltage hysteresis is suppressed on the first cycle and hole states are present at the end of charge, as

demonstrated by O K-edge X-ray absorption spectroscopy (XAS), indicative of electron-holes on oxygen.[21] However, there is a divergence of opinion on the nature of these electron-hole states and, particularly, whether they are localised or delocalised.[27–31] This question is important for a full understanding of O-redox chemistry and the development of O-redox cathodes without voltage hysteresis.

Here we exploit the suppressed metal migration in $Na_{0.6}[Li_{0.2}Mn_{0.8}]O_2$ to investigate the nature of the hole states on O^{2-} and follow their evolution with time, using a combination of high resolution RIXS, ^{17}O NMR, DFT and SQUID magnetometry. The data show that the electron-holes and unpaired electrons created upon oxidation of the oxide ions are delocalised. In $Na_{0.6}[Li_{0.2}Mn_{0.8}]O_2$, there are two coordination environments for O, O-Mn_2 and O-Mn_3. We show oxidation occurs on the O-Mn_2, which unlike O-Mn_3, possesses a non-bonding O2p orbital just under the Fermi level. The O-Mn_3 remains relatively unchanged from the pristine state. Over a period of days, the oxidised O ions with delocalised hole states condense to form molecular O_2, in accordance with the gradual loss of the high voltage plateau seen in the electrochemistry. These results provide the first direct evidence of the nature of the delocalised electron-holes that form on the O^{2-} ions when O^{2-} is oxidised in a battery cathode. The majority of O-redox compounds possess the honeycomb arrangement of ions on the transition metal layers and this is composed of the O-Mn_2 environment exclusively. Therefore, by examining $Na_{0.6}[Li_{0.2}Mn_{0.8}]O_2$ where the O-Mn_2 are separated into ribbons by O-Mn_3 and condensation of O to O_2 is slowed, we have been able to capture the nature of electron-hole states formed initially when O^{2-} ions are oxidised and to show that the electron-holes are delocalised.

Main

The O-redox cathode, $Na_{0.6}[Li_{0.2}Mn_{0.8}]O_2$, was prepared following the method in our previous report.[21] $Na_{0.6}[Li_{0.2}Mn_{0.8}O_2]$ exhibits a layered structure of P2 stacked layers of O^{2-} ions (ABBA stacking), where Li- and Mn occupy octahedral sites between a pair of O^{2-} layers forming TMO_2 slabs separated by layers of Na-ions, Figure 1a. The Li and Mn ions are ordered in a ribbon arrangement throughout the TMO_2 layers. In this configuration, the oxide ions are bonded to three Mn ions in the ribbons, that separate oxide ions bonded to two Mn ions (and one Li) in a 2:3 ratio within the TMO_2 slabs.

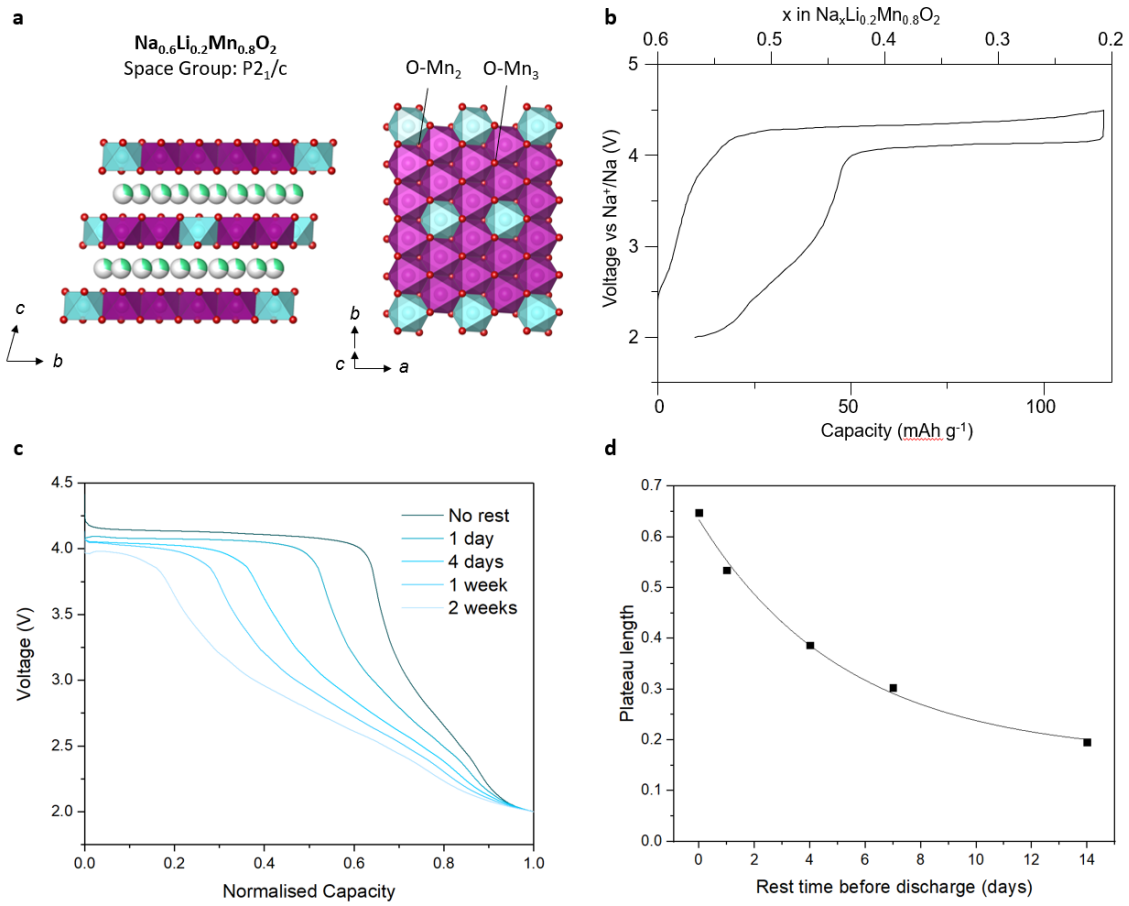

Figure 1. Structure and electrochemistry of $Na_{0.6}[Li_{0.2}Mn_{0.8}]O_2$. **a** Crystal structure of $Na_{0.6}[Li_{0.2}Mn_{0.8}]O_2$ viewed parallel and perpendicular to the layers. O^{2-} ions (red) adopt P2 stacking, ABBA, Li (blue octahedra) and Mn (purple octahedra) are ordered in a ribbon arrangement within the transition metal layers and Na (green) occupies trigonal prismatic sites between the layers. **b** First-cycle charge (Na extraction) then discharge (Na reinsertion) curve for $Na_{0.6}[Li_{0.2}Mn_{0.8}]O_2$ cathodes cycled at 10 mA g^{-1}. **c** Discharge voltage curves after charging, then resting the cell for different lengths of time. Low voltage sloping capacity appears over time at the expense of the high voltage plateau. **d** Plateau length as a fraction of the entire discharge plotted against increasing rest time.

The electrochemical load curve for $Na_{0.6}[Li_{0.2}Mn_{0.8}]O_2$ on the 1st cycle in a Na-ion cell is shown in Figure 1b. Na is removed on charge and reinserted on discharge. The high voltage plateau observed on the first charge is mostly returned on subsequent discharge. Across this plateau, the charged structure nucleates and grows as a second phase at the expense of the pristine material. We have previously shown that this charged phase retains the ribbon ordering scheme but with Li ions displaced from the Mn layer to the adjacent interlayer (the TMO_2 slabs glide to form the O2 stacking and octahedral sites between the slabs, which can accommodate Li^+ as opposed to the trigonal prismatic sites of P2 (which accommodated Na) and leaving behind a ribbon ordered array of cation vacancies in the TM layers.[21]

Investigation of the electrochemical load curves as a function of time for $Na_{0.6}[Li_{0.2}Mn_{0.8}]O_2$ reveals that the discharge process changes. If the cells are left resting at the end of charge for increasing time periods, then on discharge, Figure 1c, d, the length of the plateau diminishes, giving way to a progressively lower and more sloping voltage. These observations indicate that the structure of the charged material is undergoing a time-dependent change, such that Na reinserts into a different

structure during subsequent discharge. To confirm this structural change, PXRD data were collected on electrodes that had been discharged after resting in the charged state for different lengths of time. The data show a gradual loss of ribbon ordering over similar timescales to the loss of plateau, Supplementary Figure 2. We note that there is also a slight decrease in the voltage of the discharge plateau with time. Electrochemical impedance spectroscopy (EIS) measurements in Supplementary Figure 3 show that this is at least in part due to increased cell impedance, likely from thickening SEI. There may also be a contribution from changes in the Na^+ diffusivity as the TM structure slowly reorganises.

Despite the loss of high voltage plateau over a period of days, the unrelaxed charged structure of $Na_{0.6}[Li_{0.2}Mn_{0.8}]O_2$ exists for a long enough time to permit experimental interrogation. This behaviour contrasts with that of most other known Li-rich O-redox cathodes, such as $Li_{1.2}Ni_{0.13}Co_{0.13}Mn_{0.54}O_2$, where, following O oxidation, there is no reverse plateau, and instead the entire discharge exhibits a sloping profile at lower voltage.[2,32–36] $Na_{0.6}[Li_{0.2}Mn_{0.8}]O_2$ therefore presents an opportunity to capture and examine the oxidised O species that is responsible for reversible, high voltage O-redox before the O atoms condense to O_2.

Magnetic Properties of Oxidised O

To investigate the evolution of the electron spin configuration of $Na_{0.6}[Li_{0.2}Mn_{0.8}]O_2$ during charge, we performed SQUID magnetometry measurements on the pristine material (Supplementary Figure 4) and on an electrode measured within 1 hour of charging to 4.5 V. The magnetic moments before and after charging, μ_{eff} = 3.53 μ_B and μ_{eff} = 3.52 μ_B respectively, are virtually unchanged. This indicates that the unpaired electrons created upon oxidation of the oxide ions do not contribute significantly to the magnetic moment, i.e. S = 0, implying they are delocalised in nature.

While delocalised electrons do not exhibit Curie paramagnetism, they do contribute Pauli paramagnetism to the μ_{eff}, which is several orders of magnitude weaker. Since Pauli paramagnetism is temperature independent, it should give rise to a small degree of non-linearity in the $1/\chi$ vs T plot. As shown in Supplementary Figure 5, non-linearity is observed in our data after charge and the fitting is improved by including a temperature independent term, χ_0. This value obtained for χ_0 of 8.6 x 10^{-3} cm^3 mol^{-1} (or 6.8 x 10^{-4} emu mol^{-1}) is within the range of expected values for Pauli susceptibilities (10^{-4} to 10^{-5} emu mol^{-1}) and consistent with the idea that the Pauli contribution to the paramagnetism is weak. This further supports the conclusion that the electron hole states are delocalised.

SQUID measurements were then performed on samples that had been charged to 4.5 V, extracted from their cells, and left for different periods before the SQUID measurements were made. The data in Figure 2 (extracted from Zero-Field Cooled (ZFC) data in Supplementary Figure 2), show an increase in the effective magnetic moment (μ_{eff}) indicating the emergence of unpaired electrons over time. After 2 weeks, the μ_{eff} appears to be level out at μ_{eff} = 3.61 μ_B. This is in good agreement with the theoretical value, μ_{eff} = 3.63 μ_B, calculated assuming localisation of these unpaired electrons on O_2 molecules (S = 1) trapped within the structure. Along with the increase in magnetic moment, the $1/\chi$ vs T plot also becomes more linear and the value of χ_0 decreases to 1.2 x 10^{-3} cm^3 mol^{-1} (9.5 x 10^{-5} emu mol^{-1}) after 14 days further indicating the loss of the delocalised state over time, Supplementary Figure 6. The SQUID data collected immediately after charging are invaluable in distinguishing delocalised from localised electron holes on the oxidised oxide ions. They cannot easily distinguish between localised O^- from O_2 at long relaxation times, Figure 2, whose theoretical effective magnetic moments are similar since the number of unpaired electrons per O are the same. However, combined with the RIXS data we can see that after extended time the unpaired electrons are on O_2 molecules.

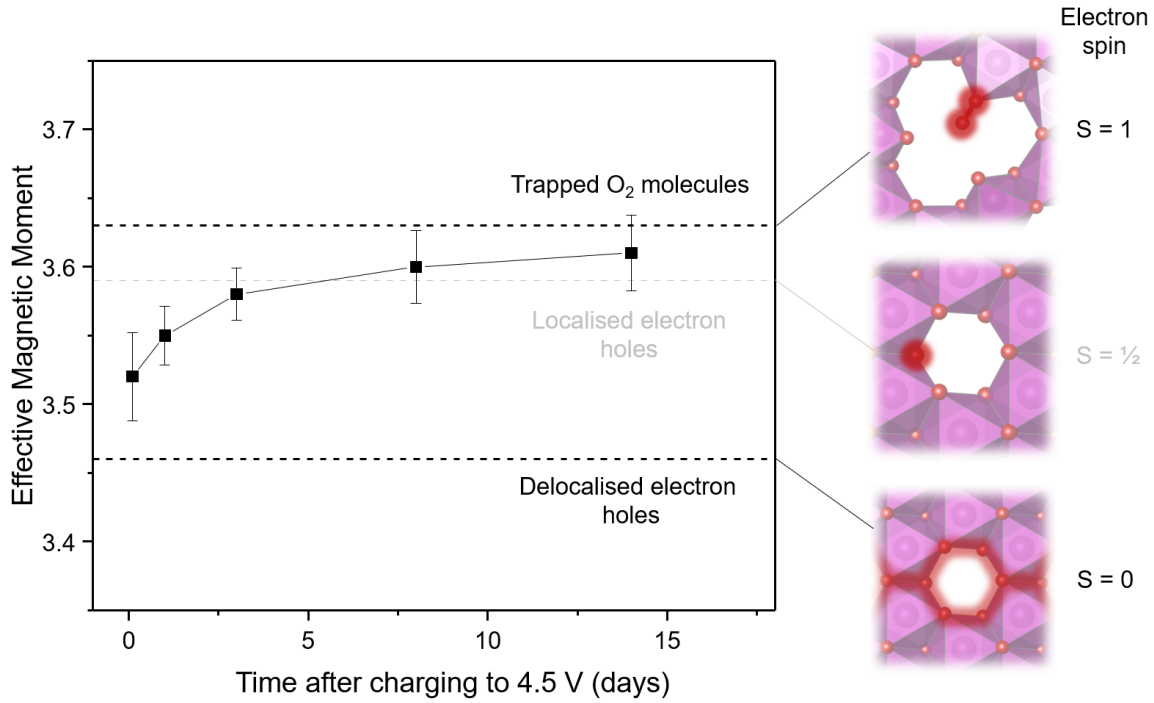

Figure 2. SQUID magnetometry. Evolution of the effective magnetic moment, μ_{eff}, for charged $Na_{0.6}[Li_{0.2}Mn_{0.8}]O_2$ with increasing rest time as measured by SQUID magnetometry. The magnetic moment measured within 1 hour of charging to 4.5 V, 3.52 μ_B, is almost identical to the pristine material, 3.53 μ_B, indicating that the hole states generated on the oxide ions on oxidation are delocalised in the O 2p band. Over time, the magnetic moment increases consistent with the localisation of electron-holes on trapped O_2 molecules which each have 2 unpaired electrons (S = 1). Note the SQUID data alone cannot easily distinguish between localised O^- and O_2 at long times but combined with the RIXS data identifying O_2 formation it can be concluded the magnetic moment after extended time is associated with O_2.

To probe the local chemical environment around the oxide ions, ^{17}O magic angle spinning (MAS) nuclear magnetic resonance (NMR) spectroscopy was employed on ^{17}O-labelled samples of $Na_{0.6}[Li_{0.2}Mn_{0.8}]O_2$. For the pristine material (Figure 3a), two distinct, well-defined chemical environments are seen centred at 2450 ppm and 2150 ppm. These can be attributed to the oxide ions bonded to two Mn (O-Mn_2) and three Mn ions (O-Mn_3), respectively. Signal fitting reveals a 58:42 intensity ratio between these two environments, in accord with the 3:2 ratio expected from the structure.

The spectrum for the charged material is shown in Figure 3b. It can be deconvoluted into two distinct chemical environments, one centred at 3750 ppm and the other at 2350 ppm in a 63:37 ratio. Again, this is consistent with the expected 3:2 ratio of O-Mn_2 and O-Mn_3 sites respectively. The substantial increase in isotropic chemical shift of the O-Mn_2 environment from the pristine to the charged state is indicative of stronger paramagnetic interactions between the O nuclei and their surroundings. We attribute this to the presence of the delocalised unpaired electrons in the O 2p band, as seen by SQUID, whose Pauli paramagnetisation effectively induces a Knight shift in the observed signal. The fact that there is only one, well-defined peak for O-Mn_2 and that the peak for O-Mn_3 barely changes chemical shift at all, supports the idea that the electron-holes form primarily on and are delocalised across the

sublattice of O-Mn_2 sites. In other words, the electron-holes are delocalised within an O2p band centred on the O of the O-Mn_2 moieties.

To further investigate the nature of the oxygen environments, we conducted a study using hybrid-exchange density functional theory (DFT) to calculate the electron spin density, ρ(0), around different O nuclei in each of the structures.[25] The calculated spin density is proportional to the chemical shift (ppm), permitting qualitative comparison to the experimental ^{17}O NMR data. The degree to which electrons are localised in these hybrid DFT calculations is determined by the electron exchange energy, which can be varied by changing the fraction of Hartree-Fock exchange (HFX).[37] First, the pristine material was modelled, lower panels in Figure 3a, based on cell parameters determined by refinement and in-plane ribbon ordering of Li and Mn as determined previously by ADF-STEM and PXRD.[21] The calculated signals for the oxygens in O-Mn_2 and O-Mn_3 environments cluster together in a narrow distribution centred around two different spin density values. The spin density calculated for O-Mn_2 is slightly higher than O-Mn_3, supporting the experimental peak assignments, Figure 3a. Next, the charged material was modelled. As shown in the panels beneath Figure 3b and in Supplementary Figure 7, the calculated spin densities for the O-Mn_2 sites are higher on average than those of the O-Mn_3, supporting the conclusion that it is the oxide ions in O-Mn_2 sites that are oxidised. The distribution of calculated spin densities for O-Mn_2 and O-Mn_3 becomes significantly wider as the % of HFX is increased as a result of increasing electron localisation. In the high HFX calculations (20% and 35%), the electron-hole density is forced to localise on alternating O–Mn_2 atoms around the ring, which would make them and the neighbouring O-Mn_3 inequivalent, and would result in several distinct environments in the NMR resonance, Supplementary Figure 8. However, this is in contrast to the observed single NMR signal. The closest agreement with the experimental data is found for the low (5 %) HFX calculations, where the electron-hole density is delocalised approximately evenly across all O–Mn_2 atoms in the rings, giving rise to a much narrower distribution of spin densities. This reinforces the conclusion that the electron-hole states are delocalised across all the O atoms coordinated by two Mn in the charged material (i.e. O-Mn_2).

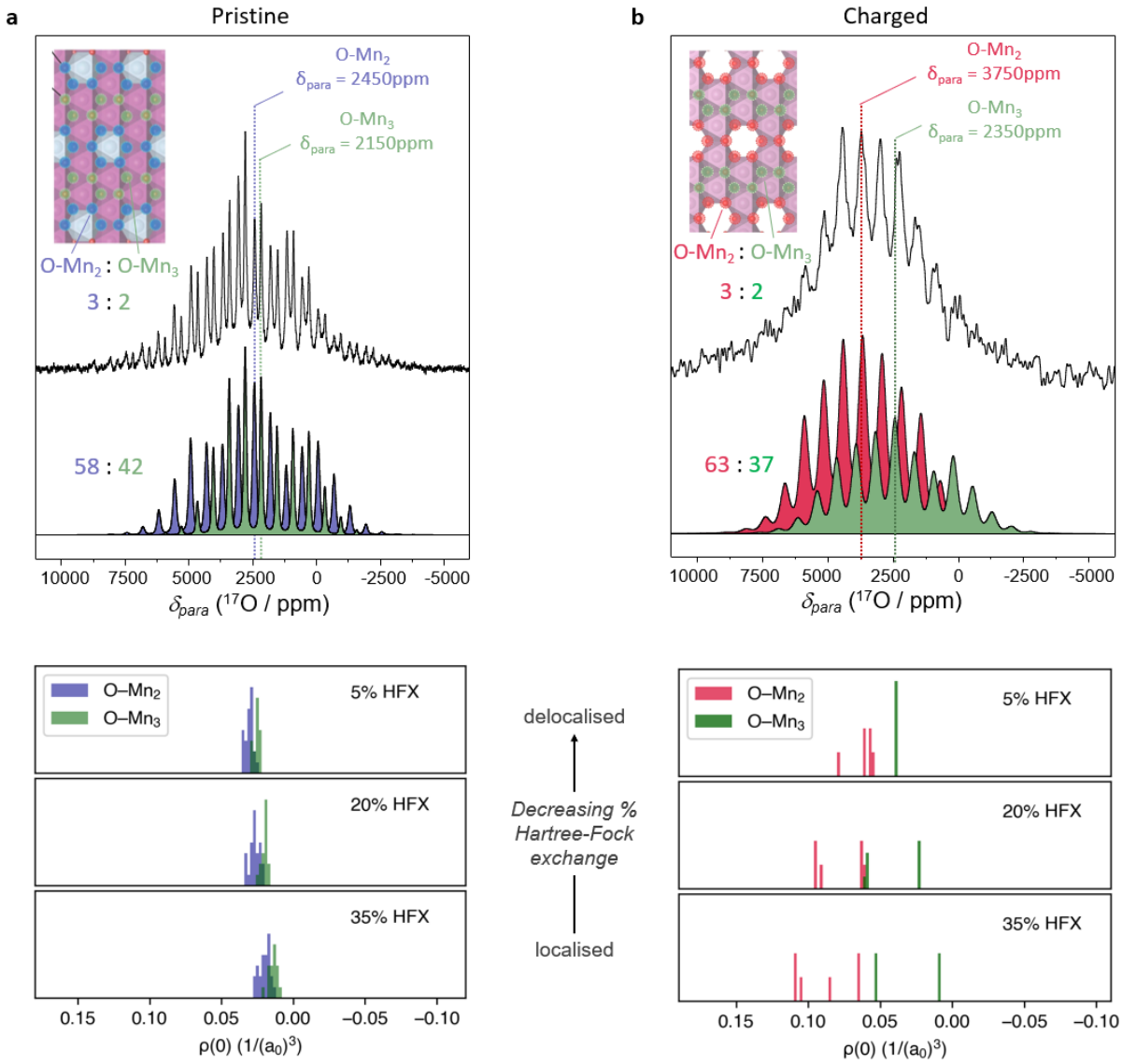

Figure 3. ^{17}O NMR spectra and DFT modelled electron spin densities. a Top - ^{17}O MAS NMR spectrum and its deconvolution for the pristine $Na_{0.6}Li_{0.2}Mn_{0.8}O_2$, fitted with 2 unique sites in a 58:42 ratio, corresponding to O coordinated by either 2Mn or 3Mn within the transition metal layer (3:2 ratio), indicated by the purple and green spectra and associated oxygens coloured similarly in the structures shown. Below, DFT calculated electron spin densities, ρ(0), at the two different oxygen positions in the structure, O-Mn_2 and O-Mn_3, with decreasing Hartree-Fock exchange (HFX) corresponding to increasing electron delocalisation. Calculated spin density, ρ(0), is directly proportional to the chemical shift, δ_{para}. O-Mn_2 exhibits a consistently higher ρ(0) for all percentages of HFX and therefore higher chemical shift than O-Mn_3, confirming the experimental peak assignment. **b** Top - ^{17}O MAS NMR spectrum and its deconvolution for charged $Na_{0.6}Li_{0.2}Mn_{0.8}O_2$. The data are fitted to a model with two unique O sites in a 63:37 ratio corresponding to the oxidised O ions in 2Mn coordination and the unoxidized 3Mn oxide ions (3:2 ratio), indicated by red and green respectively. The shift in the O-Mn spectrum on charging is due to interaction with the delocalised electrons that are located primarily on O-Mn_2 not O-Mn_3. The calculated spin densities, ρ(0), for the O–Mn_2 atoms in the charged material give better agreement to the NMR spectrum as HFX is decreased, tending towards a single value, indicating delocalisation of the electron-holes across these O-Mn_2 oxygen atoms. a_0 is the Bohr radius.

To track the changes in the oxidised O species over time, ^{17}O-labelled charged samples were measured within one hour of charging completion and then again after one- and two-week's rest. Two different NMR pulse sequences were used to detect slow relaxing (Figure 4a) and fast relaxing (Figure 4b) environments which arise due to the influence of weaker and stronger paramagnetic interactions of the O nuclei with their environment, respectively. The spectra shown in Figure 4a comprise a contribution from O-Mn_2 and from O-Mn_3 environments with isotropic chemical shifts of 3750 ppm and 2350 ppm respectively, as discussed previously. As shown in the fitted spectra (Supplementary Figure 9), the sharp O-Mn_2 and O-Mn_3 features gradually disappear over time and are replaced by a single broad feature indicative of the appearance of many unique resonances with slightly different chemical shifts. This signal broadening is consistent with an increase in disorder in the oxide environment due to the structural rearrangement that takes place.[21] Concurrently, in Figure 4b, a new, fast relaxing chemical environment emerges at 2900 ppm and grows with increasing time. This large chemical shift is consistent with that previously measured for condensed, pure O_2 as well as for molecular O_2 trapped in a different O-redox battery cathode, $Li_{1.2}Ni_{0.13}Co_{0.13}Mn_{0.54}O_2$.[18,38] Possessing two unpaired electrons, O_2 is strongly paramagnetic, resulting in a substantial relaxation enhancement and a large chemical shift. Together with the disappearance of the O-Mn_2 signal in **a**, with time, these results are consistent with the O of O-Mn_2 converting to O_2 on oxidation.

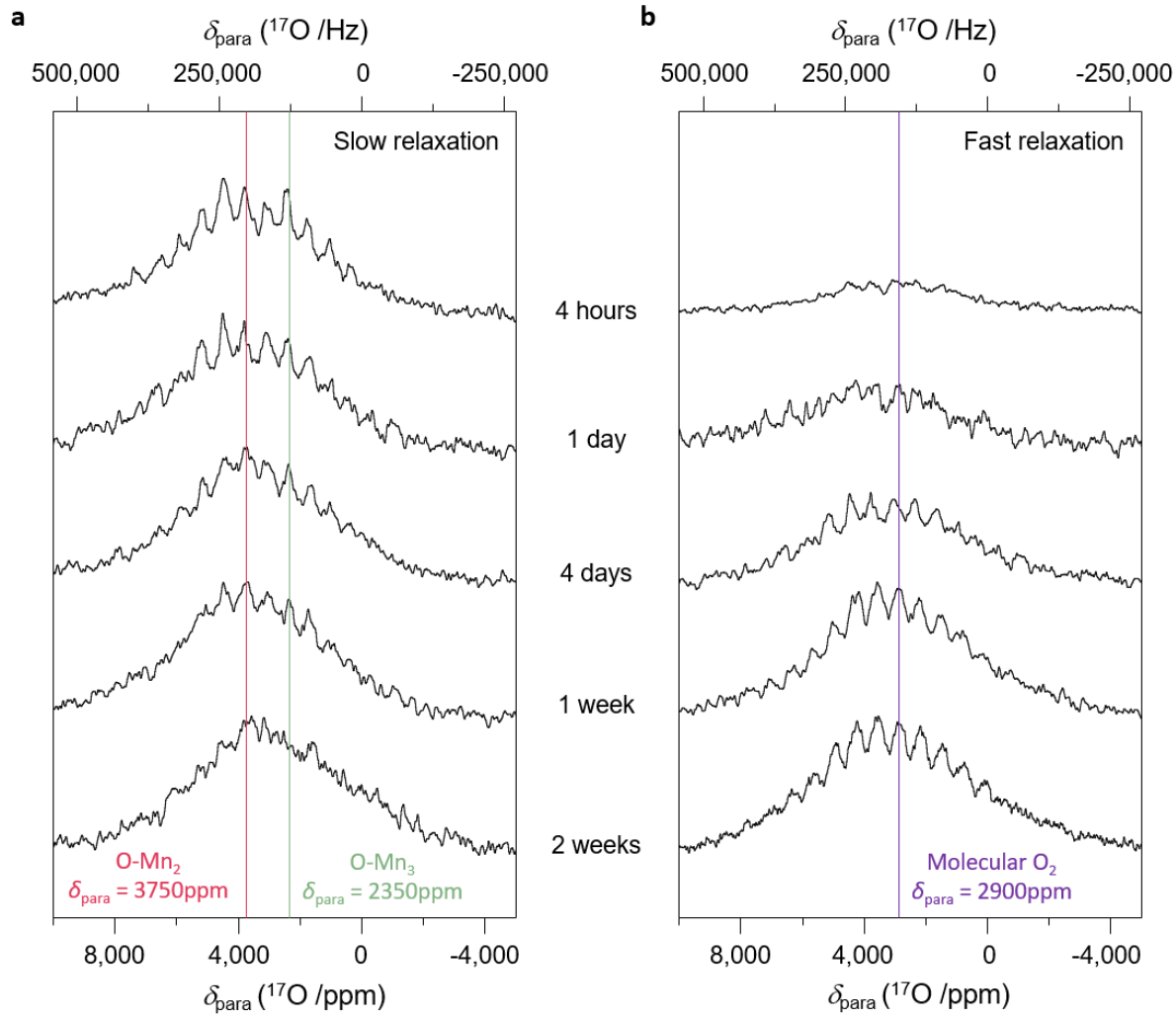

Figure 4. Time-dependent evolution of ^{17}O NMR. a Slow relaxation ^{17}O MAS NMR spectra for a charged sample of $Na_{0.6}[Li_{0.2}Mn_{0.8}]O_2$ measured over time. The charged material with resonances

associated with O-Mn_2 (red) at 3750 ppm and O-Mn_3 (green) at 2350 ppm changes with time. The O-Mn_2 resonance at 3750 ppm gradually decreases and the signal for O-Mn_3 at 2350 ppm broadens over time, indicating the appearance of multiple overlapping resonances. **b** Fast relaxation ^{17}O MAS NMR reveals another strongly paramagnetic chemical environment of O at 2900 ppm (purple) that grows in intensity over time. It is consistent the molecular O_2 trapped in bulk cathodes.[18,38]

Spectroscopic Characterisation of Oxidised O

A spectroscopic study of the O K-edge was conducted to probe the electronic structure of O in the charged material following one day and one month's rest. High resolution resonant inelastic X-ray scattering (RIXS) and soft XAS were employed to measure the filled and empty O 2p states respectively. O RIXS maps were obtained by collecting the emission spectrum (x-axis) at a series of different excitation energies (y-axis) across the O K-edge Figure 5a. In the one day sample, a feature at 528 eV is evident in the XAS, assigned previously to the electron-holes formed on lattice O during charge.[21,27] At this excitation energy in the RIXS map, an intense energy loss feature centred 1 eV below the elastic line is observed, associated with the remaining electrons in the partially depleted band of O-Mn_2 states. There is also evidence of emission intensity between 0-1 eV energy loss, linking this feature with the elastic line, suggesting there are electronic states in this band all the way up to the Fermi level, supporting the conclusion that these new O 2p electronic states are delocalised.

In comparison, for the one-month sample, there is a clear decrease in the intensity of the 528 eV features seen in XAS and the RIXS map, and evidence of some growth in intensity in the region of 531.5 eV. The feature at 531.5 eV was probed further by conducting RIXS line scans at this excitation energy. The resulting RIXS line scans in Figure 5b reveal two main features that are shared by molecular O_2 gas,[39] a broad peak at 7.5 eV energy loss and a series of sharp peaks between an energy loss of 0-2 eV, both of which grow in intensity over time. These features and their intensity change with time are also seen in the RIXS maps in Figure 5a and highlighted by the dotted regions. The decrease of the feature at 528 eV and increase at 531.5 eV over time, reflect the decay of the oxidised oxide ions to trapped molecular O_2, in accord with the SQUID and ^{17}O NMR data. Despite the change in intensity of the features, the peak spacing in the progression remains the same as shown in Figure 5c and by the Birge-Sponer plot, Figure 5d. These peaks arise from transitions to different vibrational energy levels of the O_2 molecule and are consistent with RIXS data collected on trapped O_2 previously in other systems.[18,36,40] The lack of change in spacing with time indicates that the bonding nature of the O_2 remains constant.

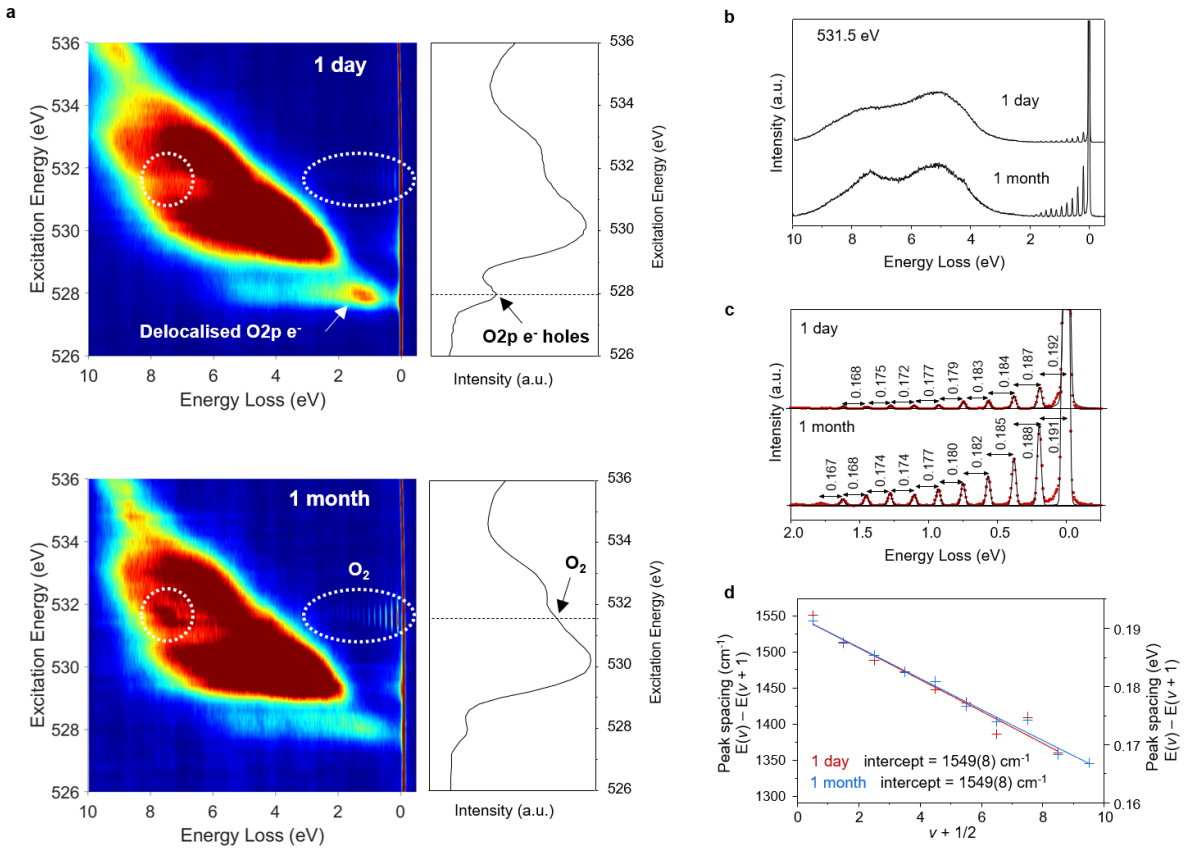

Figure 5. Oxygen K-edge Spectroscopy. a RIXS maps (left) and XAS spectra (right) of the O K-edge for $Na_{0.6}Li_{0.2}Mn_{0.8}O_2$ collected 1 day and 1 month after charging. XAS plotted sideways to relate to the RIXS maps **b** RIXS line scans obtained at the resonance energy for the vibrational peaks arising from O_2 (531.5 eV). The electron-hole feature appears intense after 1 day in the XAS and RIXS but diminishes over time. Concurrently, features attributed to molecular O_2 increase in intensity with time implying the delocalised electron-holes gradually condense to form stable O_2 molecules. **c** Peak spacings between the vibrational peaks. **d** Birge–Sponer plot showing the linear decrease in peak spacing characteristic of an anharmonic oscillating diatomic. v, vibrational quantum number. Y-intercept values indicate a fundamental vibrational frequency close to that of molecular O_2 (1556 cm^{-1}).

Discussion

Establishing the reaction pathway of the O-redox process has been complicated by the fact that transition metal migration and O–O dimerization occurs following the oxidation of oxide ions in the majority of known oxide cathodes materials. Here, by using $Na_{0.6}[Li_{0.2}Mn_{0.8}]O_2$ as a model material, with a ribbon-ordered transition metal layer superstructure that slows transition metal migration, we can capture and study the oxidised O species before O_2 formation in greater depth than before. Ultimately, O-redox that arrests at oxidised lattice O rather than O_2 is required in order to deliver a cathode that is truly reversible in terms of voltage; therefore, understanding the nature of these O states is important.

The combined SQUID, ^{17}O NMR, DFT and RIXS results demonstrate that the hole states formed on oxidised oxide ions are delocalised and occur on the oxide ions coordinated to only two transition metal ions (O-Mn_2). Such oxide ions possess O 2p orbitals directed towards a Li^+ cation vacancy in the transition metal layers rather than a Mn ion, as in the case of O-Mn_3.[7] These essentially non-bonding

O2p states place electrons in these orbitals at the top of the valence band just below the Fermi level, Figure 6a and therefore available for oxidation.[7,21,41]

Removal of electrons from these non-bonding O 2p orbitals generates a partially filled band of O 2p states which sits across the Fermi Level, Figure 6b. The density of states plot computed with 5% Hartree-Fock exchange, Supplementary Figure 10, which gives the closest agreement to the ^{17}O NMR, predicts a band shape that is consistent with the RIXS measurement. The O-Mn_2 configuration is the only O coordination that exists in the majority of O-redox layered compounds that exhibit the honeycomb superstructure. The value of examining $Na_{0.6}[Li_{0.2}Mn_{0.8}]O_2$ is that by separating the regions of O-Mn_2 by ribbons of O-Mn_3, the transformation of O to O_2 is sufficiently inhibited that we can examine the holes states and demonstrate delocalisation that will also occur in the honeycomb compounds, Supplementary Figure 11.

Our findings are relevant to Li-rich cathodes as removal of electrons from oxide ions should in the first instance form electron holes whatever the cations, e.g. Na or Li, in the alkali ion layer. However, in most materials TM migration is facile, forming voids that allow the oxygen hole states to condense to form trapped molecular O_2, giving rise to voltage hysteresis. Even though our results show that delocalised holes on oxidised oxide ions are more stable than localised holes, realising O-redox cathodes without voltage hysteresis will require materials that prevent TM migration. This is demonstrated by the fact that the material does gradually form O_2 and our previous calculations showed the energy stabilisation that accrues from the formation of the dioxygen bond. Therefore, the focus must turn to finding materials in which TM migration can be avoided, thus preserving the hole states and the high voltage plateau for many cycles.

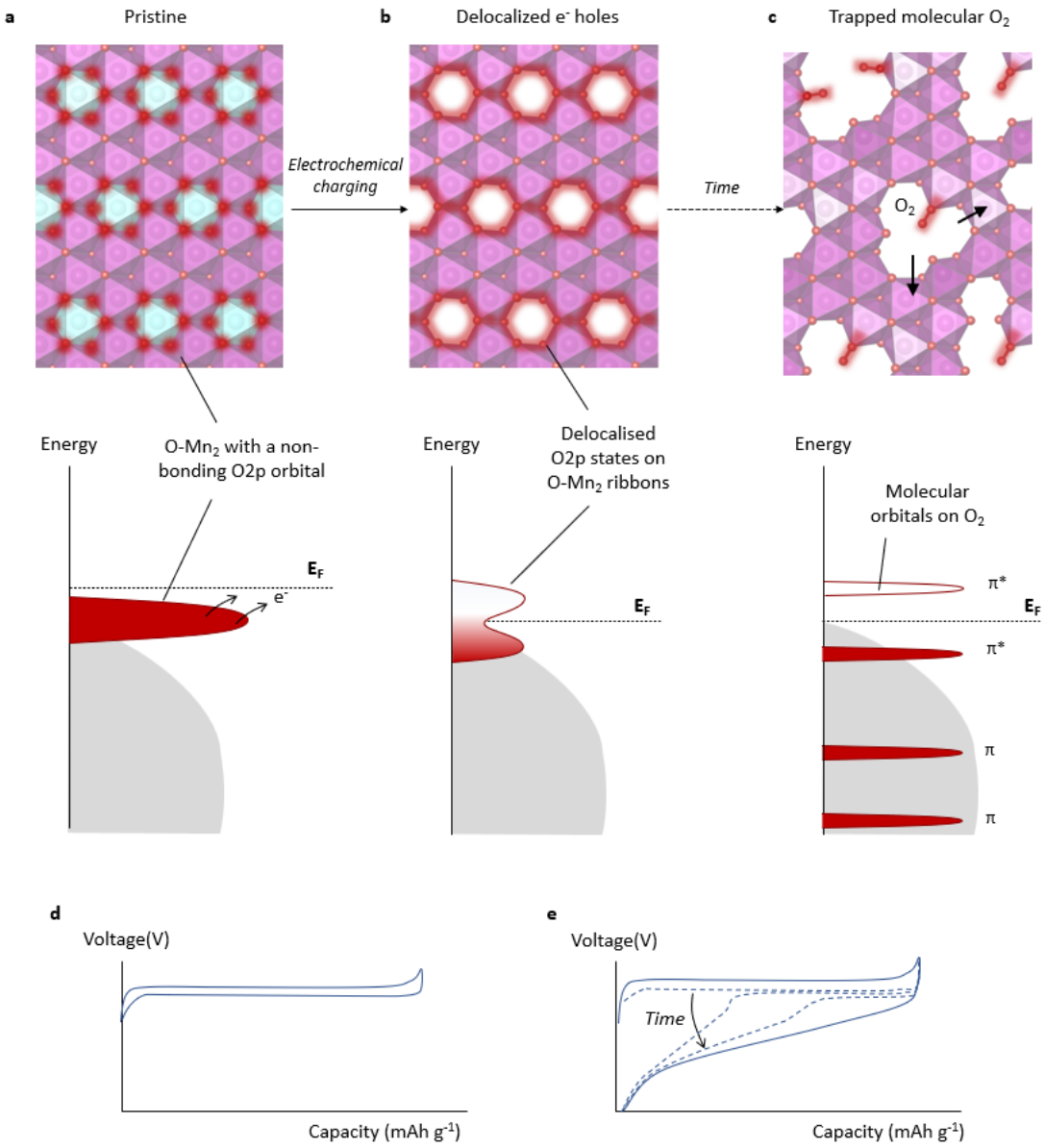

Figure 6. Delocalised electron-holes on O. Structural schematics illustrating **a** the pristine structure, **b** the charged structure with delocalised electron-holes on O-Mn_2 and **c** a charged structure after condensation of the delocalised holes to form molecular O_2. Below each structure are schematic density of states plots illustrating the changes to the O2p states near the Fermi Level. **d** Electrochemical load curve for stable electron-holes on O. **e** Loss of plateau and onset of hysteresis with time as electron-holes condense to molecular O_2.

Conclusion

The removal of electrons from the oxide ions in O-redox cathode materials on charging results in the formation of delocalised electron-holes in the O 2p band. These are delocalised across the O 2p states directed towards vacant cation sites in the transition metal layer coordinated by only two Mn ions (O-Mn_2). This coordination occurs on every oxygen in honeycomb ordered materials, which make up the majority of layered O-redox cathodes. By studying $Na_{0.6}[Li_{0.2}Mn_{0.8}]O_2$, where these O2p states are separated into O-Mn_2 ribbons by regions of O-Mn_3, transition metal migration is suppressed therefore

suppressing O_2 formation and we are able to capture these states on oxidised O and show that they are delocalised in nature. Furthermore, we follow these delocalised electron-hole states over time as they condense to form molecular O_2 which is trapped within the structure due to the slow transition metal disordering. Our results show that the unpaired electrons formed on the oxidised oxide ions are more stable if delocalised than localised. The slow evolution to form O_2 and our previous calculations that show a strong stabilisation by formation of covalent dioxygen bond in O_2, indicate that delocalisation alone will not avoid voltage hysteresis. Ultimately, O-redox cathodes that form hole states on O and do not transform into O_2 are desirable to deliver truly reversible cathodes (i.e. with the same high voltage on discharge as charge), understanding the nature of the reversible O-redox reaction could unlock a new generation of high energy density battery cathodes.

Methods

Materials Preparation. $Na_{0.6}Li_{0.2}Mn_{0.8}O_2$ was prepared as described previously.[21] Intimately mixed precursors were heated to 800 C under flowing O_2 for 12 hours, then cooled at 2 C min^{-1} to room temperature. ^{17}O labelled samples were prepared following the same calcination procedure but in an atmosphere of O_2 gas (CortecNet >70 atom% ^{17}O).

Electrochemical Measurements. Self-supporting cathode films of $Na_{0.6}Li_{0.2}Mn_{0.8}O_2$ were prepared by grinding the as-synthesised material with acetylene black and polytetrafluoroethylene in an 8:1:1 mass ratio in a pestle and mortar followed by calendaring to a thickness of ~100 µm. Cathodes were assembled into coin cells with 1M $NaPF_6$ (Kishida) in PC (Merck) used as the electrolyte and Na metal foil as the counter electrode. Cells were disassembled and the electrodes rinsed with dry dimethylcarbonate prior to *ex situ* characterisation. All handling was performed under inert atmosphere (< 0.1 ppm H_2O and O_2). Electrochemical charge-discharge cycling was carried out using a Maccor Series 4000.

EIS Measurements. After galvanostatic charging to 4.5 V, EIS measurements were recorded once every 24 hours for 7 days on a Biologic VMP3 with EIS capability over a frequency range of 100 mHz to 10 MHz. Each EIS measurement lasted ~8.5 mins.

Resonant Inelastic X-ray Scattering. RIXS spectra were obtained at the I21 beamline at Diamond Light Source. Samples were transferred to the spectrometer using a vacuum transfer suitcase to avoid air exposure and were pumped down to UHV and left to fully degas overnight. RIXS maps were measured in 0.2 eV energy increments from 526 eV to 536 eV at 3 different sample locations summed together. RIXS line scans were recorded at the resonance energy for molecular O_2 at fifteen different sample locations and averaged together.

Powder X-ray diffraction. PXRD patterns were obtained for the as-prepared materials using a Cu source Rigaku SmartLab diffractometer equipped with a Ge(220) double bounce monochromator and a Hypix 2D detector. Reitveld profile refinements were performed using the GSAS suite of programs. Ex-situ PXRD was collected on a Cu source Rigaku Miniflex benchtop diffractometer housed within an N_2-filled glovebox (O_2 < 0.1 ppm, H_2O < 0.1 ppm).

SQUID magnetometry. Samples were weighed, packed into plastic capsules, and then loaded into a Quantum Design MPMS 3 Magnetometer where they were pumped down under vacuum. Zero-field cooled measurements were performed between 100-300 K under a magnetic field of 500 Oe. The error bars represent the compounded fractional errors from sample weighing and the Na content determined electrochemically (i.e. molecular mass).

Solid-state ^{17}O MAS NMR spectroscopy. All ^{17}O magic angle spinning (MAS, υ_R = 37037 Hz) solid state NMR were completed at 9.45 T ($\upsilon_0{}^{17}O$ = 54.25 MHz) using a Bruker Advance III HD spectrometer and a 1.9 mm double air bearing MAS probe. The achieved spectra were referenced to H_2O at 0 ppm. All spectra were recorded using a Hahn echo ($\pi/2$-τ-π-τ) sequence, where τ is $1/\upsilon_R$ and $\pi/2$ is 250 kHz, the resultant FID is processed as a half echo. These spectra were completed with relaxation times of 100 ms (slow relaxation) and 1 ms (rapid relaxation) to give greater contrast between the oxide and O_2 environments.

DFT calculations. Density functional theory (DFT) calculations to assign the ^{17}O NMR environments were performed using the CRYSTAL17 code, which implements local Gaussian basis sets.[42] Previous studies have indicated that hybrid functionals give a reasonably accurate description of the unpaired spin density and the nuclear position for transition metal oxides, and have shown that the description of the spin density depends on the amount of Hartree Fock exchange (HFX) included in the hybrid functionals.[37] In general terms, as the HFX varies, the nature of the wavefunction can be considered to vary from delocalised to localised; pure DFT with no HFX produces more delocalised wavefunctions, whereas increasing the HFX results in increasingly localised wavefunctions. In this work, we adopted a benchmarking approach, in which all the properties are calculated with seven hybrid functionals based on the B3LYP parameterisation, varying HFX from 5% to 35%, in steps of 5%.

Using a similar procedure for computing ^{17}O NMR parameters described in Ref[43] we first performed a full geometry optimisation of each structure with each functional, using standard double-zeta basis sets taken from the CRYSTAL online repository (https://www.crystal.unito.it/basis-sets.php), denoted Mn_pob_DZVP_rev2, O_pob_DZVP_rev2, Li_pob_DZVP_rev2 and Na_pob_DZVP_rev2. For the calculation of spin density at the nuclear positions, single point energy calculations were performed by replacing the DZVP O basis set only with a modified version of a more extended IGLO-III basis set for O, available in original form from the Basis Set Exchange (https://www.basissetexchange.org/). To obtain the modified IGLO-III basis set, the most diffuse s and p orbitals were removed, yielding (10s6p2d)/[6s5p2d].[44,45]

The structural model of the cathode contained 20 formula units, comprising 72 atoms for pristine $Na_{0.6}[Li_{0.2}Mn_{0.8}]O_2$ and 60 atoms for the delithiated structure with composition $Li_{0.2}Mn_{0.8}O_2$. For geometry optimisations and the calculation of hyperfine parameters, a Monkhorst-Pack mesh[46] was used to sample reciprocal space in the cells, with 36 irreducible k-points. To model the partially filled Na layer in pristine $Na_{0.6}[Li_{0.2}Mn_{0.8}]O_2$, 10 different random distributions of Na ions in the unit cell (containing 72 atoms) with P1 symmetry were assessed. A small energetic difference between models of <5 meV f.u.$^{-1}$ was found, consistent with a disordered arrangement of Na. The most stable structure was selected to perform the calculation of the unpaired spin density (ρ(0)) at the ^{17}O nuclear positions.

The calculations were converged with an energy tolerance for the self-consistent field procedure of 10^{-7} Hartree, and with Coulomb and exchange integral series tolerances set at 10^{-7}, 10^{-7}, 10^{-7}, 10^{-7} and 10^{-14} for the Coulomb overlap and penetration, exchange overlap and *g* and *n* series exchange penetration, respectively. Structural optimizations were performed with a ferromagnetic alignment of ions, in which the atomic positions and unit cell parameters were allowed to fully relax. The structural optimizations were performed with a quasi-Newtonian algorithm and structural parameters converged using the standard convergence criteria in CRYSTAL17.

References

1. Lu, Z. & Dahn, J. R. Understanding the Anomalous Capacity of Li/Li[$Ni_xLi_{(1/3-2x/3)}Mn_{(2/3-x/3)}$]$O_2$ Cells Using In Situ X-Ray Diffraction and Electrochemical Studies. *J Electrochem Soc* **149**, A815–A815 (2002).

2. Lu, Z., Beaulieu, L. Y., Donaberger, R. A., Thomas, C. L. & Dahn, J. R. Synthesis, Structure, and Electrochemical Behavior of Li[$Ni_xLi_{1/3-2x/3}Mn_{2/3-x/3}$]$O_2$. *J Electrochem Soc* **149**, A778 (2002).

3. Koga, H. *et al.* Reversible Oxygen Participation to the Redox Processes Revealed for $Li_{1.20}Mn_{0.54}Co_{0.13}Ni_{0.13}O_2$. *J Electrochem Soc* **160**, A786–A792 (2013).

4. Luo, K. *et al.* Charge-compensation in 3d-transition-metal-oxide intercalation cathodes through the generation of localized electron holes on oxygen. *Nat Chem* **8**, 684–691 (2016).

5. Johnson, C. S. *et al.* The significance of the Li_2MnO_3 component in 'composite' $xLi_2MnO_3{\cdot}(1-x)LiMn_{0.5}Ni_{0.5}O_2$ electrodes. *Electrochem commun* **6**, 1085–1091 (2004).

6. Saubanère, M., McCalla, E., Tarascon, J.-M. & Doublet, M.-L. The intriguing question of anionic redox in high-energy density cathodes for Li-ion batteries. *Energy Environ. Sci.* **9**, 984–991 (2016).

7. Seo, D.-H. *et al.* The structural and chemical origin of the oxygen redox activity in layered and cation-disordered Li-excess cathode materials. *Nat Chem* **8**, 692–697 (2016).

8. Gent, W. E. *et al.* Coupling between oxygen redox and cation migration explains unusual electrochemistry in lithium-rich layered oxides. *Nat Commun* **8**, 2091 (2017).

9. Tran, N. *et al.* Mechanisms Associated with the "Plateau" Observed at High Voltage for the Overlithiated $Li_{1.12}(Ni_{0.425}Mn_{0.425}Co_{0.15})_{0.88}O_2$ System. *Chemistry of Materials* **20**, 4815–4825 (2008).

10. Assat, G. *et al.* Fundamental interplay between anionic/cationic redox governing the kinetics and thermodynamics of lithium-rich cathodes. *Nat Commun* **8**, 2219 (2017).

11. Yabuuchi, N. *et al.* Origin of stabilization and destabilization in solid-state redox reaction of oxide ions for lithium-ion batteries. *Nat Commun* **7**, 13814 (2016).

12. Zhao, E. *et al.* Local structure adaptability through multi cations for oxygen redox accommodation in Li-Rich layered oxides. *Energy Storage Mater* **24**, 384–393 (2020).

13. Zhang, M. *et al.* Pushing the limit of 3d transition metal-based layered oxides that use both cation and anion redox for energy storage. *Nature Reviews Materials 2022* 1–19 (2022).

14. Li, M. *et al.* Cationic and anionic redox in lithium-ion based batteries. *Chem Soc Rev* **49**, 1688–1705 (2020).

15. Yu, Y. *et al.* Towards controlling the reversibility of anionic redox in transition metal oxides for high-energy Li-ion positive electrodes. *Energy Environ Sci* **14**, 2322–2334 (2021).

16. Gent, W. E., Abate, I. I., Yang, W., Nazar, L. F. & Chueh, W. C. Design Rules for High-Valent Redox in Intercalation Electrodes. *Joule* **4**, 1369–1397.

17. Assat, G. & Tarascon, J. M. Fundamental understanding and practical challenges of anionic redox activity in Li-ion batteries. *Nat Energy* **3**, 373–386 (2018).

18. House, R. A. *et al.* First-cycle voltage hysteresis in Li-rich 3d cathodes associated with molecular O_2 trapped in the bulk. *Nat Energy* **5**, 777–785 (2020).

19. House, R. A. *et al.* The role of O_2 in O-redox cathodes for Li-ion batteries. *Nature Energy* **6**, 781-789 (2021).

20. House, R. A. *et al.* Detection of trapped molecular O_2 in a charged Li-rich cathode by Neutron PDF. *Energy Environ Sci* **15**, 376–383 (2022).

21. House, R. A. *et al.* Superstructure control of first-cycle voltage hysteresis in oxygen-redox cathodes. *Nature* **577**, 502–508 (2020).

22. Du, K. *et al.* Exploring reversible oxidation of oxygen in a manganese oxide. *Energy Environ Sci* **9**, 2575–2577 (2016).

23. Gao, A. *et al.* Topologically protected oxygen redox in a layered manganese oxide cathode for sustainable batteries. *Nature Sustainability **5**, 214-224* (2021).

24. Rong, X. *et al.* Structure-Induced Reversible Anionic Redox Activity in Na Layered Oxide Cathode. *Joule* **2**, 125–140 (2018).

25. Eum, D. *et al.* Coupling structural evolution and oxygen-redox electrochemistry in layered transition metal oxides. *Nature Materials* **21**, 664–672 (2022).

26. Kim, E. J. *et al.* Importance of Superstructure in Stabilizing Oxygen Redox in P3-$Na_{0.67}Li_{0.2}Mn_{0.8}O_2$. *Adv Energy Mater* **12**, 2102325 (2022).

27. Abate, I. I. *et al.* Coulombically-stabilized oxygen hole polarons enable fully reversible oxygen redox. *Energy Environ Sci* **14**, 4858–4867 (2021).

28. Kitchaev, D. A., Vinckeviciute, J. & van der Ven, A. Delocalized Metal-Oxygen π-Redox Is the Origin of Anomalous Nonhysteretic Capacity in Li-Ion and Na-Ion Cathode Materials. *J Am Chem Soc* **143**, 1908–1916 (2021).

29. Tsuchimoto, A. *et al.* Nonpolarizing oxygen-redox capacity without O-O dimerization in Na2Mn3O7. *Nature Communications* **12**, 631 (2021).

30. Sudayama, T. *et al.* Multiorbital bond formation for stable oxygen-redox reaction in battery electrodes. *Energy Environ Sci* **13**, 1492–1500 (2020).

31. Zhao, C., Liu, H., Geng, F., Hu, B. & Li, C. Stable electronic structure related with $Mn^{4+}O^{-\bullet}$ coupling determines the anomalous nonhysteretic behavior in $Na_2Mn_3O_7$. *Energy Storage Mater* **48**, 290–296 (2022).

32. Sathiya, M. *et al.* Reversible anionic redox chemistry in high-capacity layered-oxide electrodes. *Nat Mater* **12**, 827–835 (2013).

33. McCalla, E. *et al.* Visualization of O-O peroxo-like dimers in high-capacity layered oxides for Li-ion batteries. *Science* **350**, 1516–1521 (2015).

34. Hong, J. *et al.* Metal-oxygen decoordination stabilizes anion redox in Li-rich oxides. *Nat Mater* **18**, 256–265 (2019).

35. Yabuuchi, N. *et al.* A new electrode material for rechargeable sodium batteries: P2-type $Na_{2/3}[Mg_{0.28}Mn_{0.72}]O_2$ with anomalously high reversible capacity. *J. Mater. Chem. A* **2**, 16851–16855 (2014).

36. House, R. A. *et al.* Covalency does not suppress O_2 formation in 4d and 5d Li-rich O-redox cathodes. *Nat Commun* **12**, 2975 (2021).

37. Clément, R. J. *et al.* Spin-transfer pathways in paramagnetic lithium transition-metal phosphates from combined broadband isotropic solid-state MAS NMR spectroscopy and DFT calculations. *J Am Chem Soc* **134**, 17178–17185 (2012).

38. Dundon, J. M. ^{17}O NMR in liquid O_2. *J Chem Phys* **76**, 2171–2173 (1982).

39. Arhammar, C. *et al.* Unveiling the complex electronic structure of amorphous metal oxides. *Proceedings of the National Academy of Sciences* **108**, 6355–6360 (2011).

40. Boivin, E. *et al.* Bulk O_2 formation and Mg displacement explain O-redox in $Na_{0.67}Mn_{0.72}Mg_{0.28}O_2$. *Joule* **5**, 1267–1280 (2021).

41. ben Yahia, M., Vergnet, J., Saubanère, M. & Doublet, M.-L. Unified picture of anionic redox in Li/Na-ion batteries. *Nat Mater* **18**, 496–502 (2019).

42. Dovesi, R. *et al.* Quantum-mechanical condensed matter simulations with CRYSTAL. *Wiley Interdiscip Rev Comput Mol Sci* **8**, e1360 (2018).

43. Seymour, I. D. *et al.* Characterizing Oxygen Local Environments in Paramagnetic Battery Materials via ^{17}O NMR and DFT Calculations. *J Am Chem Soc* **138**, 9405–9408 (2016).

44. Kim, J. *et al.* Linking local environments and hyperfine shifts: A combined experimental and theoretical ^{31}P and ^{7}Li solid-state NMR study of paramagnetic Fe(III) phosphates. *J Am Chem Soc* **132**, 16825–16840 (2010).

45. Middlemiss, D. S., Ilott, A. J., Clément, R. J., Strobridge, F. C. & Grey, C. P. Density functional theory-based bond pathway decompositions of hyperfine shifts: Equipping solid-state NMR to characterize atomic environments in paramagnetic materials. *Chemistry of Materials* **25**, 1723–1734 (2013).

46. Monkhorst, H. J. & Pack, J. D. Special points for Brillouin-zone integrations. *Phys Rev B* **13**, 5188 (1976).

Acknowledgements

The authors are indebted to the EPSRC, the Henry Royce Institute for Advanced Materials (EP/R00661X/1, EP/S019367/1, EP/R010145/1, EP/L019469/1) and the Faraday Institution (FIRG007, FIRG008, FIRG016) for financial support. We thank the HEC Materials Chemistry Consortium (EP/R029431/1) for supercomputer facilities. We acknowledge Diamond Light Source for time on I21 under proposal MM25589-1. This project was supported by the Royal Academy of Engineering under the Research Fellowship scheme.

Author Contributions

R.A.H. planned and conducted the synthesis and characterisation work. R.A.H. and S.C. planned and conducted the SQUID measurements. R.A.H. prepared the ^{17}O labelled samples and G.J.R performed and fitted the ^{17}O MAS NMR. R.A.H. and J-J.M. in close collaboration with M.G-F., A.N., and K.Z. conducted the RIXS and XAS measurements. K.M. conducted the DFT computation and NMR shift modelling with the support of B.M. and M.S.I. R.A.H. and P.G.B. wrote the manuscript with contributions from all authors.

Competing Interest Statement

The authors declare no competing interests.

Data Availability Statement

Supporting research data is available under the following DOIs: